Materials Advances

ROYAL SOCIETY OF CHEMISTRY

PAPER

View Article Online
View Journal | View Issue

Cite this: *Mater. Adv.*, 2025, 6, 8497

Synthesis and breathing behaviour of a new member of the fluoride-substituted gallium MIL-53 metal–organic framework solid-solution series

A. R. Bonity J. Lutton-Gething, †[a] Ruxuan Lan,[a] Yongkang Huang,[a] Thomas J. Duddles,[a] Carlo Bawn,[a] Daniel Lee,[b] George F. S. Whitehead[a] and Martin P. Attfield *[a]

Received 11th July 2025,
Accepted 8th October 2025

DOI: 10.1039/d5ma00742a

rsc.li/materials-advances

A new member of the fluoride-substituted gallium MIL-53 metal–organic framework $[Ga(OH)_{1-x}F_x(bdc)]$ (bdc^{2-} = 1,4-benzenedicarboxylate) solid-solution series, $[Ga(OH)_{0.80}F_{0.20}(bdc)]$ (**1**), is reported that extends the series to $[Ga(OH)_{1-x}F_x(bdc)]$ ($x \leq 0.20$). The framework fluoride content is 33% greater than the previously reported highest framework fluoride-containing gallium MIL-53 $[Ga(OH)_{0.85}F_{0.15}(bdc)]$ and is achieved using a novel HF-free route. The effects of the additional μ_2-F^- bridging anions in the framework on the breathing behaviour of **1** are profound compared to those previously reported for [Ga(OH)(bdc)] and $[Ga(OH)_{0.85}F_{0.15}(bdc)]$. Large pore-**1** (lp-**1**) does not transform to narrow pore-**1** (np-**1**) over the entire 500–100–500 K temperature range investigated and np-**1** undergoes transformation to lp-**1** on heating from 400 K to 500 K at a suitably fast heating rate. Both results indicate the greater stability of lp-**1** relative to np-**1**. The combined use of heating and guest water desorption/adsorption is sufficient to allow **1** to exhibit a full breathing cycle. Overall, this work demonstrates the ability to tune the breathing properties of a MIL-53 MOF through the method of fluoride incorporation into the μ_2-bridging anion framework site and should be a methodology applicable to engineer the breathing and other behaviours of many MOFs in a controlled manner.

1. Introduction

Metal–organic frameworks (MOFs) form an expansive family of nanoporous materials with numerous interesting properties and are being commercially applied for storage and separation processes.[1,2] Within the family of MOFs, a small subset display significant framework flexibility in response to stimuli including, temperature, pressure, and host–guest interactions.[3,4] The flexible nature of these frameworks leads to potential applications that differ from the more commonly observed rigid frameworks, such as selective flexible absorbents,[5] and as substrates for the controlled delivery of drugs where guest-specific pore dimensions results in slow release of drug molecules.[6]

The quintessential group of flexible MOFs is the MIL-53 family, which is a series of isostructural frameworks with the general formula: [MX(bdc)] where M = Al^{3+},[7,8] Sc^{3+},[9] V^{3+},[10] Cr^{3+},[11] Fe^{3+},[12] Ga^{3+},[13,14] or In^{3+},[15] X = $(OH)^-$ or F^- and bdc^{2-} = 1,4-benzenedicarboxylate. These frameworks are formed from MO_4X_2 octahedra which extend through μ_2-X bridging anions to form 1-dimensional inorganic chains of *trans*-corner sharing MO_4X_2 octahedra, as shown in Fig. 1a. These chains are interconnected by bdc^{2-} linkers to form the 3-dimensional framework that contain 1-dimensional pores extending along the direction of the inorganic chain as shown in Fig. 1b. MIL-53 can exhibit frameworks with different unit cell or void volumes, often referred to as large pore (lp), intermediate pore (int) and narrow pore (np) structures with associated reduction in unit cell and void volume respectively.[16] Transition between some or all of these possible structures, as exemplified in Fig. 1b, is induced by different stimuli.[3,4] The thermoresponsive flexing or "breathing" behaviour of MIL-53 frameworks can be modified by changing the M cation,[16] incorporation of a mixture of different M cations,[17] modification of the bdc^{2-} linker,[18] incorporation of a mixture of different bdc^{2-}-based linkers,[19] or a mixture of these strategies.[20] Minimal attention, however, has been paid to the impact of modifying the μ_2-X bridging anion in the inorganic chain of these frameworks. Increasing the fluoride content in the inorganic component of other MOFs is found to impart desirable

[a] *Department of Chemistry, School of Natural Sciences, The University of Manchester, Oxford Road, Manchester, M13 9PL, UK. E-mail: m.attfield@manchester.ac.uk*
[b] *Department of Chemical Engineering, School of Engineering, The University of Manchester, Oxford Road, Manchester, M13 9PL, UK*
† Current address: School of Chemistry, The University of Birmingham, Edgbaston, Birmingham, B15 2TT, UK.

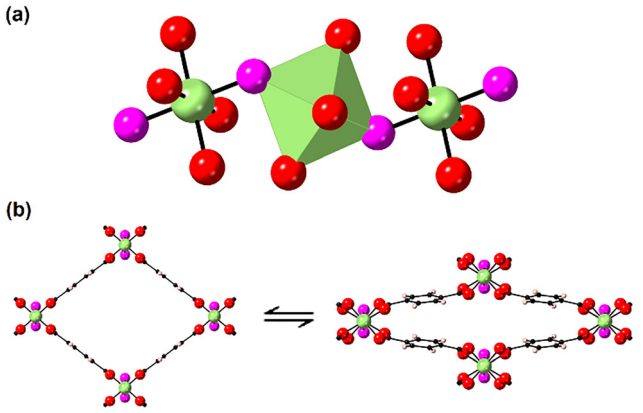

Fig. 1 The constituent 1-dimensional inorganic chains of *trans*-corner sharing MO_4X_2 octahedra of [MX(bdc)] MIL-53 MOFs (a), and the lp (left) and np (right) forms of the flexible MIL-53 framework (b). Structures are represented in polyhedral and ball-and-stick modes. Atom key: M^{3+} = green, μ_2-X = pink, O = red, C = black, H = light pink.

properties such as improved water stability[21] and to increase selectivity in gas adsorption processes, for example that of CO_2 over other gases.[22] Incorporation of fluoride into the μ_2-X site of the inorganic chain of MIL-53 has been shown to modify the flexibility of the framework. Completely replacing μ_2-$(OH)^-$ for μ_2-F^- converts [AlX(bdc)] from a MOF that can flex under the action of various stimuli to an essentially inflexible framework with a lp structure.[8,23] A marked difference is also observed in the uptake of alcohols by [Fe(OH)(bdc)]·H_2O compared to [$Fe(OH)_{0.8}F_{0.2}$(bdc)]·H_2O. The latter transitions through an intermediate phase during alcoholic solvent exchange that is not observed in the absence of μ_2-F^-.[24] More recently, variable temperature single crystal studies of [Ga(OH)(bdc)] and [$Ga(OH)_{0.85}F_{0.15}$(bdc)] (Ga : F ratio derived directly from reported Ga and F elemental analysis data)[25] has shown that a partial substitution of μ_2-$(OH)^-$ for μ_2-F^- can result in the lp form being favoured over a greater range of temperatures, and a low temperature np to lp expansion accompanied by the adsorption of N_2(g) within the pores.[26] The latter examples demonstrate that small μ_2-F^- fractions of the total μ_2-X sites in MIL-53 frameworks can significantly influence the breathing behaviour suggesting that isomorphous substitution of the μ_2-X sites in the [MX(bdc)] framework may be a route to tune the framework flexing behaviour in response to different stimuli in a designed manner.

Herein, a new member of the gallium MIL-53 family, [$Ga(OH)_{0.80}F_{0.20}$(bdc)](**1**), with increased fluorination at the μ_2-X site is reported that exhibits an incremental change in breathing behaviour compared to [Ga(OH)(bdc)] and [$Ga(OH)_{0.85}F_{0.15}$(bdc)], with a loss of thermoresponsive breathing whilst maintaining guest-induced breathing. This exemplifies the ability to tune the breathing behaviour of this MOF by controlling the nature of the μ_2-X site solely.

2. Experimental methods

2.1. Synthesis

2.1.1. 1·0.7DEF·0.08HF. All chemical reagents were used as received without further purification. GaF_3 (127 mg, 1 mmol, Alfa Asear, anhydrous, 99.85%, metals basis), terephthalic acid (H_2bdc, 0.996 g, 6 mmol, Sigma-Aldrich, 98%) and 10 mL *N*,*N*-diethylformamide (DEF, TCI Chemicals) were combined in a 23 mL Teflon lined autoclave and heated in an oven at 220 °C for 4 days. Once the reaction was complete, the autoclave was allowed to cool to room temperature and the crystalline product collected by filtration and washed with 20 mL *N*,*N*-dimethyl formamide (DMF, Fisher BioReagents) and allowed to dry in air. A typical yield for the reaction was ~20% relative to Ga.

2.1.2. 1·H_2O. 0.1–0.2 g of **1**·0.7DEF·0.08HF was activated in a tube furnace at 573 K for 5 h under a gentle flow of dry N_2(g) before exposure to atmospheric air. Heating and cooling ramp rates of 1 K min^{-1} were applied in the activation process.

2.2. Characterisation

2.2.1. Single crystal X-ray diffraction (SCXRD). Single crystal data were collected using a Rigaku FR-X dual source diffractometer with Cu K_α (λ = 1.541 Å) incident radiation, equipped with mirror monochromators. Suitable crystals were selected and mounted on MiTiGen polymer loops without the use of an adhesive agent. The temperature was controlled using a Cryostream 800 Plus applying a heating and cooling rate of 360 K h^{-1} and keeping the crystal under a constant stream of N_2(g). Data were collected and reduced using Rigaku CrystalisPro software (v49.42) and adsorption corrections performed using empirical methods based on symmetry equivalent reflections at different azimuthal angles implemented by SCALE3 ABSPACK. Using Olex2,[27] the structures were solved using either SHELXS,[28] or SHELXT.[29] SHELXL[30] was used for structural refinement implementing a least-squares minimisation routine. Structure solution and refinement were carried out against all F^2 values. In the case that a non-mereohedrally twinned crystal was selected, the twin law was determined by inspection of Ewald sphere projections, and the structure initially solved against reflections from a single component, followed by refinement against reflections from both components. All non-hydrogen atoms were refined anisotropically when possible. Hydrogen atoms were placed in calculated positions using idealised geometries and were assigned fixed occupancies and isotropic displacement parameters. Both $O(H)^-$ and F^- atoms were placed on the μ_2-X site with the occupancy of both atoms fixed to the values determined from elemental analysis and their atomic displacement parameters were set to be equivalent. Various atomic displacement and geometric parameter restraints were applied as necessary to produce the final crystal structures as detailed within the crystallographic information files (CCDC 2468139–2468142). In the case that guest molecules within the pores were observed to be highly disordered, their contribution to the crystal structure was accounted for by applying a solvent mask using the SQUEEZE routine using a probe radius of 1.2 Å.[31]

2.2.2. Powder X-ray diffraction (PXRD). Initial PXRD data were collected over 3–50° 2θ, with a step size of 0.02°, using a Phillips X'pert Pro diffractometer equipped with a sealed tube X-ray source and an X'Celerator multi-strip detector, operated

in Bragg Brentano geometry with $\frac{1}{4}$° divergence slits using Cu K_α radiation (λ = 1.541 Å).

Due to low yields, *in situ* variable temperature PXRD under dry N_2(g) was completed using the diffractometer and heater described for the SCXRD experiments. In these experiments the powder was packed into 0.3 mm or 0.5 mm diameter glass capillaries. The capillary was then glued upright into a stub and cut to a suitable size, leaving the top of the capillary open. The capillary and stub were then placed on the goniometer and centred in the beam.

Room and 500 K temperature PXRD patterns monitoring the breathing behaviour of **1** on the removal and re-adsorption of water were collected using seven 300° ϕ scans of 300 s each over a 2θ range of 3–70° with a detector distance of 150 mm, and the beam divergence aperture set to 1.0 milli-radian. Data were converted to standard PXRD formats using the inbuilt powder diffraction extraction tool in CrysAlisPro (Rigaku v42.49). Pawley fits were performed using Topas Academic V6 software.[32] The background was accounted for using either a linear interpolate or a Chebenyov function, depending on the suitability. Peak shapes were modelled with a modified Thompson–Cox–Hastings pseudo-Voigt model (TCHZ) including axial broadening. All unit cell parameters and sample height displacement were freely refined.

2.2.3. Solid-state NMR spectroscopy. Magic angle spinning (MAS) NMR spectra were collected on Bruker 9.4 T and 16.4 T (400 and 700 MHz ^{1}H Larmor frequencies) Avance III and NEO spectrometers with 4 mm HFX and 1.3 mm HX MAS probes, respectively. ^{19}F and {^{1}H-}^{13}C cross-polarisation (CP)MAS NMR spectra were collected at a MAS frequency of 12 kHz or 50 kHz under ambient conditions. Int-**1**·0.7DEF·0.08HF and int-**1**·H_2O were loaded into 4 mm o.d. or 1.3 mm o.d. zirconia rotors under air. The rotor containing int-**1**·H_2O was activated to **1** by heating at 423 K in a vacuum oven overnight or 573 K in an oven before sealing the hot sample in the rotor with a Kel-F cap (4 mm) or Vespel base and drive caps (1.3 mm). ^{19}F and ^{13}C chemical shifts were referenced to $CFCl_3$ and TMS, respectively, using external references (PTFE tape $\delta\{^{19}F\}$ = −122.0 ppm and α-glycine $\delta\{^{13}C_{CO}\}$ = 176.03 ppm).

2.2.4. Additional characterization. ATR FTIR spectra were collected on a Bruker Alpha Platinum ATR instrument over the wavenumber range of 4000–600 cm^{-1} with a resolution of 4 cm^{-1}. Thermogravimetric curves were measured using a Mettler-Toledo TGA/DSC instrument. CHN content was measured in house using a Thermo FlashSmart CHN instrument. Metal and fluorine contents were measured by Medac Ltd (UK) using Schöniger flask oxygen combustion followed by ion chromatography.

3. Results and discussion

3.1. Int-1·0.7DEF·0.08HF

Int-**1**·0.7DEF·0.08HF (a = 6.6882(8) Å^3, b = 11.009(3) Å^3, c = 18.045(2) Å^3, β = 92.75(1)°, V = 1327.1(4) Å^3) crystallises in the monoclinic $I2/a$ space group (see SI, Table S1) with an unit cell volume between the np- and lp-unit cell extremes and the expected MIL-53 framework topology as shown in Fig. 2. Int-**1**·0.7DEF·0.08HF was produced as a phase pure compound as indicated by the excellent Pawley fit, using these crystal data compared to the observed PXRD data as shown in Fig. S1. It was not possible to determine the location of the guest molecules within the void volume of int-**1**·0.7DEF·0.08HF due to their significant disorder. Application of a solvent mask to account for the significant electron density observed within the void volume suggested the presence of 110 electrons per unit cell which are in the centre of the pores as shown in the residual electron density contour map shown in Fig. S2.

The ^{19}F MAS NMR spectrum of int-**1**·0.7DEF·0.08HF is shown in Fig. 3a. The peak observed at $\delta\{^{19}F\}$ = −137 ppm corresponds well to that expected for μ_2-F^- anions in this type of environment.[33] This peak has a clear shoulder upfield (more negative) at $\delta\{^{19}F\}$ = −140 ppm; variations in the interactions between μ_2-F^- anions and the guest molecules within the pores may lead to the observation of more than one F environment. Previous reports suggest that uneven distributions of guest molecules within the pores and distortions in the structure caused by host–guest interactions can result in the broadening of isotropic peaks.[34] There is an additional sharp peak observed at $\delta\{^{19}F\}$ = −127 ppm, which, due to the intensity and narrowness of the peak, is attributed to free fluoride ions or HF within the pores. The elemental analysis, given in Table S2, indicates that there is a Ga : F ratio of 1 : 0.28 in int-**1**·0.7DEF·0.08HF of which 0.08F is present as guest species within the pores and 0.20 is present in the framework (*vide infra*). The former is chemically accounted for as HF to allow charge balance in the compound.

The ATR FTIR spectrum of int-**1**·0.7DEF·0.08HF shown in Fig. S3a indicates that there are DEF molecules within the void volume due to the presence of the carbonyl stretch at 1668 cm^{-1}. The presence of DEF within the pores is further confirmed by the {^{1}H-}^{13}C cross-polarisation MAS NMR spectrum shown in Fig. S4a where characteristic peaks corresponding to DEF are observed at $\delta\{^{13}C\}$ = 162, 34 and 29 ppm.

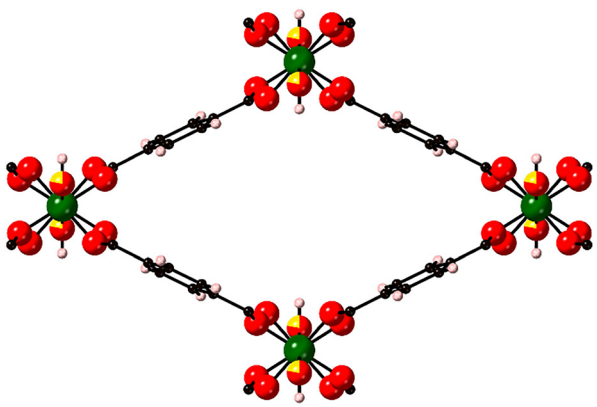

Fig. 2 The framework of int-**1**·0.7DEF·0.08HF viewed along the pore direction. The μ_2-X bridging site is shown with the proportions of $(OH)^-$ and F^- determined from elemental analysis. Atom key: Ga = green, O = red, F = yellow, C = black, H = pink.

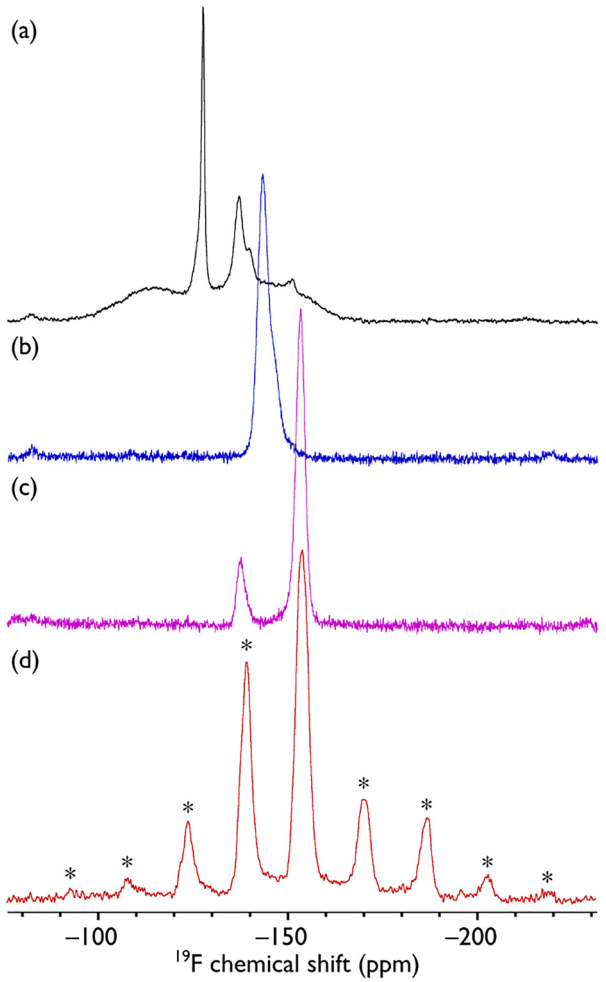

Fig. 3 ^{19}F MAS NMR spectra of (a) int-**1**·0.7DEF·0.08HF, (b) int-**1**·H_2O, (c) lp-**1**/np-**1** and (d) np-**1**. (a)–(c) were recorded at 16.4 T using a MAS frequency of 50 kHz whereas (d) was recorded at 9.4 T using a MAS frequency of 6 kHz to facilitate fitting of the anisotropy ($\delta_{11}/\delta_{22}/\delta_{33}$ = −127/−144/−191 ppm). Spinning sidebands are marked with *.

These results suggest the presence of DEF and reaction by-product HF are present in the void volume of **1**. The TGA trace shown in Fig. S5a shows a steady mass loss of approximately 23% between 303 and 630 K. A second mass loss of 33% is observed to start at approximately 713 K which is attributed to the loss of bdc linkers and the decomposition of the framework. The 23% mass loss corresponds to a chemical formula **1**·0.7DEF·0.08HF assuming it is attributable to HF and DEF only. The presence of the DEF and HF species in the void volume of **1** differs from that reported in the as-synthesised MIL-53 compound [AlF(bdc)]·0.09[$H_2N(CH_3)_2F$]·0.09HF where HF and dimethylammonium fluoride were found within the void volume.[8] [AlF(bdc)]·0.09[$H_2N(CH_3)_2F$]·0.09HF was synthesized under similar conditions to int-**1**·0.7DEF·0.08HF except DMF was used as the synthesis solvent. The difference in pore guest species may reflect the difference in stability of DEF and DMF under the reaction conditions used.

3.1.1. Int-1·H_2O. Int-**1**·H_2O (a = 6.6570(15) Å, b = 7.436(2) Å c = 19.182(4) Å, β = 96.15(2)°, V = 944.1(4) Å^3) crystallises in the monoclinic $I2/a$ space group (see Table S3) with an unit cell volume between the np- and lp-unit cell extremes and the structure shown in Fig. 4a. Int-**1**·H_2O was produced as a phase pure compound as indicated by the Pawley fit to the observed PXRD data obtained using this unit cell shown in Fig. S6. One crystallographically distinct H_2O molecule is found within the pores that is disordered over two possible positions as shown in Fig. 4b and separated by possible O···O distances of 2.50(4) Å and 3.35(4) Å along the channel. The H_2O molecules hydrogen bond to the μ_2-bridging $(OH)^-$ with a O(μ_2-$(OH)^-$)···O(H_2O) distance of 2.76(3) Å. The crystal structure of int-**1**·H_2O is reminiscent of the int-[$Ga(OH)_{0.9}F_{0.1}$(bdc)]·H_2O structure (Cc, a = 19.66 Å, b = 7.64 Å, c = 6.67 Å, β = 103.88°, V = 973.4 Å^3) reported by Boutin *et al.*,[14] but differs significantly when compared to the crystal structures of isostructural int-[Ga(OH)(bdc)]·H_2O and int-[$Ga(OH)_{0.85}F_{0.15}$(bdc)]·H_2O ($P2_1/c$, a = 6.6662(3) Å, b = 14.7953(10) Å, c = 19.2119(8) Å, β = 96.366(4)°, V = 1883.16(17) Å^3).[26] The quality of the diffraction data collected for int-**1**·H_2O was insufficient to solve and refine the crystal structure in the lower symmetry, larger unit cell of int-[Ga(OH)(bdc)]·H_2O and int-[$Ga(OH)_{0.85}$ $F_{0.15}$(bdc)]·H_2O.

The ^{19}F MAS NMR spectrum of int-**1**·H_2O is shown in Fig. 3b and has a peak at $\delta\{^{19}F\}$ = −143 ppm with a shoulder at $\delta\{^{19}F\}$ = −146 ppm (3 : 2). These can be assigned to the expected single crystallographic fluoride environment found in the framework interacting with two different H_2O sites or it may indicate that the structure of int-**1**·H_2O has an isostructural crystal structure

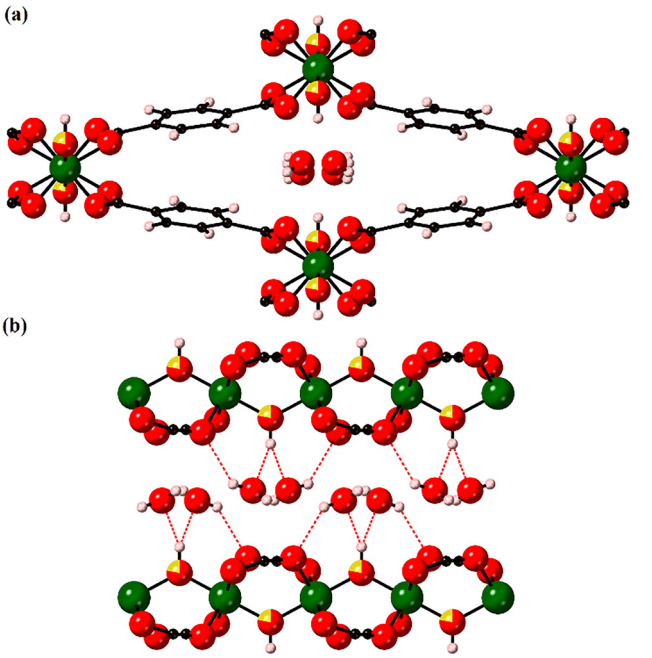

Fig. 4 (a) Int-**1**·H_2O viewed along the pore direction showing the location of water molecules within the pores. (b) Int-**1**·H_2O viewed perpendicular to the inorganic chain of **1** showing the possible hydrogen-bonding interactions between the H_2O molecules and the framework O or H atoms. Only one H_2O molecule is found in either of the two possible H_2O molecule positions at each μ_2-X bridging anion site. Atom key: Ga = green, O = red, F = yellow, C = black, H = pink.

to int-[Ga(OH)(bdc)]·H_2O and int-[$Ga(OH)_{0.85}F_{0.15}$(bdc)]·H_2O where there are two closely related crystallographic fluoride environments that interact with different H_2O molecules.[26] For the latter, this would suggest preferential occupancy of the two different crystallographic environments by fluorine.

The ATR FTIR spectrum of int-**1**·H_2O shown in Fig. S3b confirms the presence of water as evidenced by the observation of peaks at 3313 cm^{-1} and 1620 cm^{-1} corresponding to $\nu_3(H_2O)$ and $\nu_2(H_2O)$ modes. The $\nu_1(H_2O)$ mode expected at 3525 cm^{-1} is masked.[13] Additional peaks that were previously obscured for int-**1**·0.7DEF·0.08HF are observed at 3601, 1125 and 965 cm^{-1} and attributed to ν(OH), and two δ(OH) bands respectively indicating the presence of μ_2-$(OH)^-$ groups.[13] The position of the ν(OH) band indicates that the μ_2-$(OH)^-$ group is hydrogen bonded to water molecules within the pores. The spectrum of int-**1**·H_2O shown in Fig. S3b also confirms the absence of DEF from the void volume as indicated by the loss of the characteristic DEF C═O stretch at 1668 cm^{-1} (Fig. S3a and c). The $\{^1H\text{-}\}^{13}C$ cross-polarisation MAS NMR spectrum of int-**1**·H_2O (shown in Fig. S4b) supports the absence of DEF and the shifted peaks of the framework C atoms ($\delta\{^{13}C\}$ = 175, 136, and 130 ppm) suggest a different structure and guest-binding interactions compared to int-**1**·0.7DEF·0.08HF.

The TGA trace of int-**1**·H_2O shown in Fig. S5b gives a mass loss of 5.0% (calculated 6.6%) between 303–369 K. The absence of other mass losses before sample decomposition at 703 K indicates that all other guest molecules have been removed. The elemental analyses given in Table S4 indicates that there is a Ga : F ratio of 1 : 0.20 in int-**1**·H_2O and provides good agreement with the full chemical formula of int-**1**·H_2O. The reduction in fluorine content in int-**1**·H_2O compared to int-**1**·0.7DEF·0.08HF supports the presence of fluorine in the pores of the framework that is removed upon activation. There is no evidence of the associated ^{19}F resonance of free F^- or HF in int-**1**·H_2O (Fig. 3b).

3.1.2. Thermoresponsive and water induced breathing behavior. A single crystal of int-**1**·H_2O was selected and SCXRD data were collected at 100 K to reconfirm the crystal structure of int-**1**·H_2O and the presence of water within the pores. The crystal was then heated in 100 K steps to 500 K with the crystal structure or unit cell parameters determined at each temperature. The framework of int-**1**·H_2O remained hydrated at 200 K, but at 300 K it was not possible to determine the crystal structure due to a decrease in crystallinity and significant movement of the crystal during collection which continued despite multiple attempts to re-centre the crystal and restart the data collection. The unit cell of the crystal structure at 300 K had a slightly reduced unit cell volume (*I*2/*a*, a = 6.723(4) Å, b = 7.116(10) Å, c = 19.358(12) Å, β = 95.58(6)°, V = 922(2) $Å^3$) compared to that at 100 K (full details are given in Table S5). By 400 K, an increase in the crystal quality enabled the crystal structure to be determined which showed that it had transformed to the np-form, np-**1**, with a further reduction of the unit cell volume (*I*2/*a*, a = 6.677(4) Å, b = 6.955(12) Å, c = 19.368(11) Å, β = 95.83(6)°, V = 895(2) $Å^3$) and the loss of H_2O from the pores as seen in Fig. 5a and Tables S5, S6. The

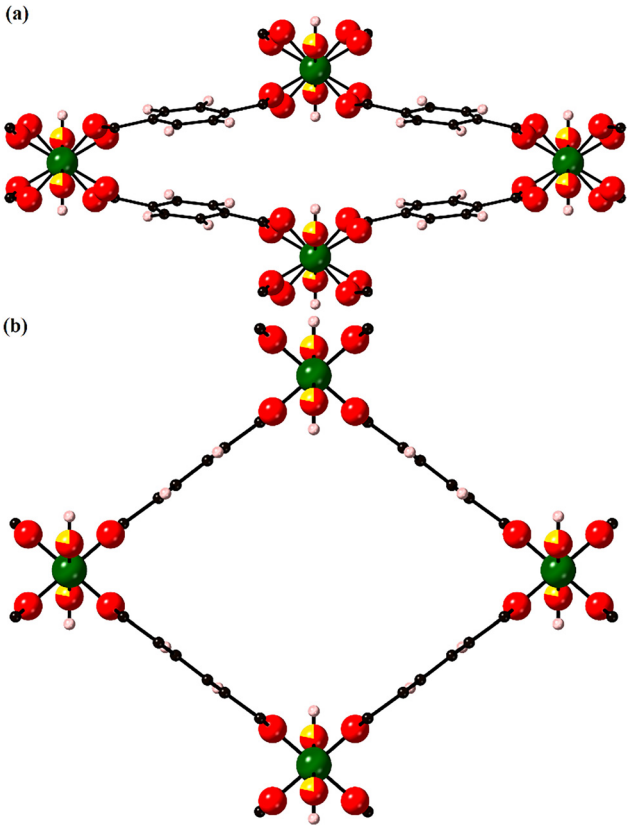

Fig. 5 (a) np-**1** at 400 K viewed along the pore direction. (b) lp-**1** at 500 K viewed along the pore direction. Atom key: Ga = green, O = red, F = yellow, C = black, H = pink.

structure of np-**1** closely matches the previously reported crystal structures of np-[Ga(OH)(bdc)] and np-[$Ga(OH)_{0.85}F_{0.15}$(bdc)].[26] The ^{19}F MAS NMR spectrum of np-**1** generated by activating int-**1**·H_2O under vacuum at 423 K for 16 h is shown in Fig. 3d. A single isotropic peak at $\delta\{^{19}F\}$ = −153 ppm is present, matching the single crystallographic fluoride environment in the framework and verifying that interactions with guest molecules within the pores was the likely cause for the asymmetric peaks in the ^{19}F MAS NMR spectra of int-**1**·0.7DEF·0.08HF and potentially int-**1**·H_2O (Fig. 3a and b).

A phase change from np-**1** to lp-**1** was observed on heating further to 500 K with an accompanying increase in the unit cell volume of 63%, and a change of the crystal system from monoclinic to orthorhombic (*Imma*, a = 16.529(2) Å, b = 6.6846(11) Å, c = 13.175(3) Å, V = 1455.6(5) $Å^3$). The crystal structure of lp-**1** is shown in Fig. 5b, with associated crystal data provided in Tables S5 and S7. Application of a solvent mask to the structure determined at 500 K indicated that there was no residual electron density remaining in the pores, confirming that the framework had been completely activated. The opening of the framework to lp-**1** is accompanied by an increase in the overall intensity ($I/\sigma > 10$) and sharpness of the observed diffraction peaks indicating that the np–lp phase transition results in improved crystallinity.

The ^{19}F MAS NMR spectrum of int-**1**·H_2O heated in air at 573 K for 16 h is shown in Fig. 3c. It has two peaks, one aligning

with np-**1** ($\delta\{^{19}F\}$ = −153 ppm) and the other aligning with the framework F of int-**1**·0.7DEF·0.08HF ($\delta\{^{19}F\}$ = −137 ppm). This latter peak is thus attributable to the single crystallographic fluoride environment expected in lp-**1**. There appears to be a trend for the ^{19}F MAS NMR spectra that the chemical shift decreases as the shortest pore dimension decreases, noting that the ^{19}F chemical shift of the μ_2-F^- anions is also very sensitive to its binding with guest molecules in the pores. This trend is opposite for the ^{13}C NMR chemical shifts of the aromatic-CH of the organic linkers in guest-free **1** (see Fig. S4) and is caused by the rotation of the linker that increases as the shortest pore direction decreases. The ^{13}C NMR chemical shifts of the carboxyl and *ipso* C do not move except for int-**1**·0.7DEF·0.08HF and this indicates that the carboxylate is involved in DEF-binding, as inferred in the residual electron density map (Fig. S2). This highlights the sensitivity of NMR spectroscopy to changes in environment experienced by the MOF during flexing and guest adsorption.

The single crystal was then cooled and heated in 50 K steps in the range 500–100–500 K and crystal structures were obtained at each temperature. The lp-**1** phase is maintained throughout the heating and cooling cycle and no further phase transitions were observed as indicated in Fig. 6. The unit cell volumes of lp-**1** varied over a small 1430–1463 Å^3 range over these temperatures. A significant amount of disordered electron density is observed in the pore at 100 K which is attributed to the sorption of ~4N_2 per Ga forming lp-**1**·~4N_2. A similar amount of adsorbed N_2 was found in lp-[Ga(OH)$_{0.85}$F$_{0.15}$(bdc)]·~4N_2 at 100 K suggesting similar behaviour and void volumes for both compounds.[26] Similar calculations on all the structures from 500–100–500 K indicated a steady increase in adsorbed N_2 from 500 K to 200 K followed by a rapid increase to 100 K. The void electron density content is given in Table S8 and shown in Fig. S7. The single crystal was finally cooled to 300 K and allowed to sit in ambient air for 5 h. The crystal remained as lp-**1** with no H_2O entering the void volume of the framework.

To investigate if room temperature adsorption of H_2O would transform lp-**1** to int-**1**·H_2O a powdered sample of int-**1**·H_2O was activated *in situ*, by heating to 500 K under a constant stream of N_2(g), to form lp-**1** with a very small proportion of np-**1** also present (see Fig. S8). The sample was then cooled to room temperature followed by exposure to air for 17 h at room temperature that caused the sample to convert to int-**1**·H_2O as shown in Fig. 7. The sample displayed the same behaviour during a second cycle of this treatment confirming that reversible breathing behaviour is possible for this material when triggered by the adsorption/desorption of guest H_2O molecules so proving that reversible flexing is possible for **1**.

The thermoresponsive behaviour of a second single crystal of int-**1**·H_2O was studied to try to determine the np-lp transition temperature more accurately. The crystal structure of int-**1**·H_2O at 289 K under air was initially determined confirming the hydration of the crystal. The crystal was then placed under dry N_2(g) at 300 K and structure determination confirmed it dehydrated to np-**1** within 30 min (see Table S9). The crystal was heated directly to 400 K followed by heating to 500 K in 25 K steps with the crystal structure determined at each temperature. The np-**1** structure was retained over the whole temperature range and lp-**1** was not formed.

3.1.3. Comparison of the thermoresponsive and water induced breathing behaviour of 1 and other [Ga(OH)$_{1-x}$F$_x$(bdc)] compounds. The results show that the thermoresponsive behaviour of **1** is significantly different to that of previously reported [Ga(OH)(bdc)] and [Ga(OH)$_{0.85}$F$_{0.15}$(bdc)][26] as summarised in Table 1, with **1** not transforming from the lp-form to the np-form over the entire 500–100–500 K temperature range studied, whilst lp-[Ga(OH)(bdc)] and lp-[Ga(OH)$_{0.85}$F$_{0.15}$(bdc)] converted to the np-forms by the progressively lower temperatures of 300 K and 225–250 K

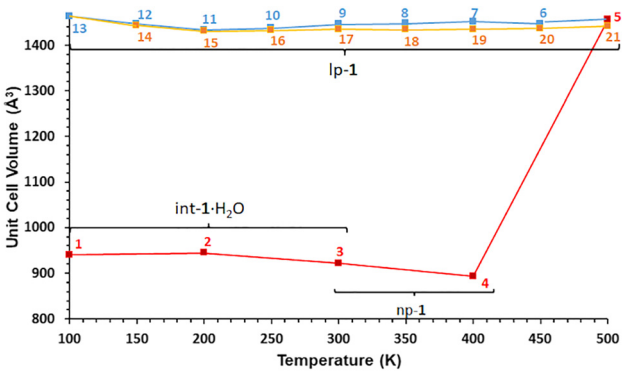

Fig. 6 Summary of the thermoresponsive behaviour of **1**·H_2O displayed as a plot of unit cell volume *versus* temperature. The order in which the crystal was heated and cooled is given by the number associated with each data point. The first heating range, the cooling range and the second heating range are represented by the red, blue and orange lines interpolating the data points respectively. The estimated standard deviations for the unit cell volumes lie in the range 0.4–1.5 Å^3.

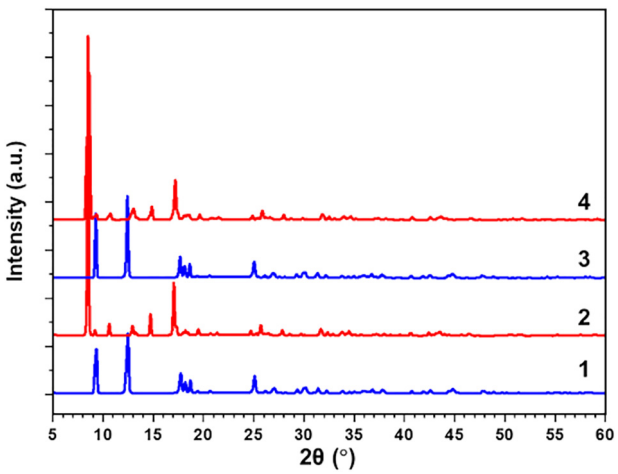

Fig. 7 PXRD patterns of int-**1**·H_2O (1) (Pawley fit shown in Fig. S6) transforming to lp-**1** (2) (Pawley fit shown in Fig. S8) on heating to 500 K, followed by reformation of int-**1**·H_2O (3) upon exposure to air for 17 h at room temperature, followed by retransformation to lp-**1** (4) on heating to 500 K again.

Table 1 Comparison of framework flexing properties of members of the $[Ga(OH)_{1-x}F_x(bdc)]$ solid-solution series

Framework flexing stimulus	$x = 0.00$	$x = 0.15$	$x = 0.20$
Thermally induced lp- to np-transformation upon cooling from 500 K to 100 K	Yes at 300 K[26]	Yes between 250–225 K[26]	No
Thermally induced np- to lp-transformation upon rapid heating	No[26]	No[26]	Yes between 400–500 K
Guest, H_2O, induced lp- to int-transformation	Yes[26,35]	Yes[26]	Yes

respectively. The difference in breathing behaviour can be attributed to the increased amount of fluoride in the μ_2-bridging anion site in the inorganic chain of **1** compared to $[Ga(OH)_{1-x}F_x(bdc)]$ ($x \leq 0.15$).[26]

This behaviour is directly related to the greater destabilisation of np-**1** relative to lp-**1** than that seen in $[Ga(OH)_{1-x}F_x(bdc)]$ ($x \leq 0.15$) effectively reducing the energy required for a np- to lp-conversion. Consequently, the lp-form is observed over a greater temperature range. The destabilisation of np-**1** relative to lp-**1** derives from the additional strain produced through distortion of the chains of gallium-centred octahedra that contain more $GaO_4(OH)F$ or GaO_4F_2 octahedra and any subtle accompanying change in dispersive forces involving the organic linkers on transforming from the lp- to the np-form. The additional strain due to such distortions will stem from the electronic differences of the F^- and $(OH)^-$ ions and any subsequent effects they may have on framework bonding. The absence of thermoresponsive flexibility observed in **1** compared to [Ga(OH)(bdc)] and $[Ga(OH)_{0.85}F_{0.15}(bdc)]$ suggests that there is a non-linear relationship between the fluoride content of these compounds and the lp- to np-transition temperature for the contracting breathing behaviour with only a relatively small increase in the overall fluoride content removing the pore contracting breathing response of the [GaX(bdc)] framework.

The additional fluoride content in **1** compared to $[Ga(OH)_{1-x}F_x(bdc)]$ ($x \leq 0.15$) also produces observed differences in the single crystal thermoresponsive expanding breathing behaviour for the np- to lp-transition with np-**1** transforming to lp-**1** on heating from 400 K to 500 K at a relative fast heating rate but not at a slower heating rate. [Ga(OH)(bdc)] and $[Ga(OH)_{0.85}F_{0.15}(bdc)]$ do not transform from the np- to the lp-form at a slow or flash heating rate, again indicating the additional destabilisation of the np-form relative to the lp-form of **1** compared to the other $[Ga(OH)_{1-x}F_x(bdc)]$ ($x \leq 0.15$) compounds. The influence of the heating rate on the ability of single crystals of the Ga-MIL-53 family to undergo thermoresponsive expansion breathing behaviour has previously been observed and reported by Lutton-Gething *et al.*[26] Only flash-heating from slightly large unit cell volume int-$[Ga(OH)_{1-x}F_x(bdc)]\cdot H_2O$ ($x \leq 0.15$) phases resulted in rapid expansion to the lp-phases.

Although a thermoresponsive contraction transformation of lp-**1** was not observed in the SCXRD experiments, a contraction transformation of polycrystalline lp-**1** in response to the adsorption of guest molecules was possible as triggered by the adsorption of water. This indicates that the strong host–guest interactions formed on adsorption of H_2O provides the energetic stimulus for the contraction transformation that simple cooling does not. The combined use of heat and guest adsorption is sufficient to allow **1** to exhibit full breathing behaviour.

Stimuli dependent differences in the observed breathing behaviour of MIL-53 MOFs have been noted for iron-based MIL-53 MOFs. [Fe(OH)(bdc)] does not exhibit thermoresponsive breathing behaviour and remains in a np-form.[36] However, it can expand to the lp-form on formation of a host–guest compound by the adsorption of short chain alkenes and other organic molecules.[37,38]

4. Conclusions

This study presents a novel synthesis route to a new member of the gallium MIL-53 MOF solid-solution series, $[Ga(OH)_{0.80}F_{0.20}(bdc)]$, so extending the series to $[Ga(OH)_{1-x}F_x(bdc)]\cdot H_2O$ ($x \leq 0.20$). The framework fluoride content is 33% greater than the previously reported $[Ga(OH)_{0.85}F_{0.15}(bdc)]$ and is achieved without the use of HF in the synthesis. This demonstrates the potential to make members of MOF solution-series albeit through use of different synthesis routes to obtain members of different chemical composition. The effects on the breathing behaviour of **1** are profound compared to that reported for [Ga(OH)(bdc)] and $[Ga(OH)_{0.85}F_{0.15}(bdc)]$. This further demonstrates the ability to tune the breathing properties of a MIL-53 MOF through this method of fluoride incorporation into the μ_2-X bridging anion site to provide a material with intermediate behaviour between the extremes of exhibiting or not exhibiting thermoresponsive and guest-induced breathing as has been reported for the aluminium MIL-53 MOFs [Al(OH)(bdc)] and [AlF(bdc)] respectively.[7,8,23,39] This methodology should be applicable to potentially tune the breathing and other behaviours of other MOFs in a controlled manner.

Author contributions

ARBJLG, RL, YH synthesised the compounds; ARBJLG, GFSW collected and analysed the XRD data; ARBJLG, CB, TJD, DL collected and analysed the NMR data; ARBJLG collected and/or analysed other data; ARBJLG, CB, DL, GFSW, MPA participated in the design of experiments; ARBJLG, DL, MPA wrote the manuscript and MPA, GFSW supervised the research.

Conflicts of interest

There are no conflicts to declare.

Data availability

The data used to support the findings of this study are included within the article and Supplementary information (SI).

Supplementary information is available. See DOI: https://doi.org/10.1039/d5ma00742a.

CCDC 2468139, 2468140, 2468141 and 2468142 contain the supplementary crystallographic data for this paper.[40a–d]

Acknowledgements

ARBJLG and TJD are grateful to EPSRC and The University of Manchester for the award of DTG PhD studentships (EPSRC EP/R513131/1 and EP/W524347/1 respectively) and for funding the dual source Rigaku FR-X diffractometer (EPSRC EP/P001386/1). We also thank the EPSRC and The University of Manchester for funding the 16.4 T NMR spectrometer (EP/V007580/1) used in this work.

References

1 R. Freund, S. Canossa, S. M. Cohen, W. Yan, H. Deng, V. Guillerm, M. Eddaoudi, D. G. Madden, D. Fairen-Jimenez, H. Lyu, L. K. Macreadie, Z. Ji, Z. Yhang, B. Wang, F. Haase, C. Wöll, O. Zaremba, J. Andreo, C. Wuttke and C. S. Diercks, *Angew. Chem., Int. Ed.*, 2021, **60**, 23946–23974.
2 A. M. Wright, M. T. Kapelewski, S. Marx, O. K. Farha and W. Morris, *Nat. Mater.*, 2025, **24**, 178–187.
3 G. Férey and C. Serre, *Chem. Soc. Rev.*, 2009, **38**, 1380–1399.
4 A. Schneemann, V. Bon, I. Schwedler, I. Senkovska, S. Kaskel and R. A. Fischer, *Chem. Soc. Rev.*, 2014, **43**, 6062–6096.
5 S. Couck, J. F. M. Denayer, G. V. Baron, T. Rémy, J. Gascon and F. Kapteijn, *J. Am. Chem. Soc.*, 2009, **131**, 6326–6327.
6 P. Horcajada, C. Serre, G. Maurin, N. A. Ramsahye, F. Balas, M. Vallet-Regí, M. Sebban, F. Taulelle and G. Férey, *J. Am. Chem. Soc.*, 2008, **130**, 6774–6780.
7 T. Loiseau, C. Serre, C. Huguenard, G. Fink, F. Taulelle, M. Henry, T. Bataille and G. Férey, *Chem. – Eur. J.*, 2004, **10**, 1373–1382.
8 L. Liu, X. Wang and A. J. Jacobson, *Dalton Trans.*, 2010, **39**, 1722–1725.
9 J. P. S. Mowat, S. R. Miller, A. M. Z. Slawin, V. R. Seymour, S. E. Ashbrook and P. A. Wright, *Microporous Mesoporous Mater.*, 2011, **142**, 322–333.
10 H. Leclerc, T. Devic, S. Devautour-Vinot, P. Bazin, N. Audebrand, G. Férey, M. Daturi, A. Vimont and G. Clet, *J. Phys. Chem. C*, 2011, **115**, 19828–19840.
11 C. Serre, F. Millange, C. Thouvenot, M. Noguès, G. Marsolier, D. Louër and G. Férey, *J. Am. Chem. Soc.*, 2002, **124**, 13519–13526.
12 N. Guillou, R. I. Walton and F. Millange, *Z. Kristallogr.*, 2010, **225**, 552–556.
13 C. Volkringer, T. Loiseau, N. Guillou, G. Férey, E. Elkaïm and A. Vimont, *Dalton Trans.*, 2009, 2241–2249.
14 A. Boutin, D. Bousquet, A. U. Ortiz, F. X. Coudert, A. H. Fuchs, A. Ballandras, G. Weber, I. Bezverkhyy, J. P. Bellat, G. Ortiz, G. Chaplais, J. L. Paillaud, C. Marichal, H. Nouali and J. Patarin, *J. Phys. Chem. C*, 2013, **117**, 8180–8188.
15 E. V. Anokhina, M. Vougo-Zanda, X. Wang and A. J. Jacobson, *J. Am. Chem. Soc.*, 2005, **127**, 15000–15001.
16 F. Millange and R. I. Walton, *Isr. J. Chem.*, 2018, **58**, 1019–1035.
17 M. I. Breeze, G. Clet, B. C. Campo, A. Vimont, M. Daturi, J. M. Grenèche, A. J. Dent, F. Millange and R. I. Walton, *Inorg. Chem.*, 2013, **52**, 8171–8182.
18 A. S. Munn, R. S. Pillai, S. Biswas, N. Stock, G. Maurin and R. I. Walton, *Dalton Trans.*, 2016, **45**, 4162–4168.
19 S. Marx, W. Kleist, J. Huang, M. Maciejewski and A. Baiker, *Dalton Trans.*, 2010, **39**, 3795–3798.
20 J. Bitzer, M. Teubnerov and W. Kleist, *Chem. – Eur. J.*, 2021, **27**, 1724–1735.
21 A. Cadiau, Y. Belmabkhout, K. Adil, P. M. Bhatt, R. S. Pillai, A. Shkurenko, C. Martineau-Corcos, G. Maurin and M. Eddaoudi, *Science*, 2017, **356**, 731–735.
22 P. M. Bhatt, Y. Belmabkhout, A. Cadiau, K. Adil, O. Shekhah, A. Shkurenko, L. J. Barbour and M. Eddaoudi, *J. Am. Chem. Soc.*, 2016, **138**, 9301–9307.
23 C. Nanthamathee, S. L. Ling, B. Slater and M. P. Attfield, *Chem. Mater.*, 2015, **27**, 85–95.
24 R. I. Walton, A. S. Munn, N. Guillou and F. Millange, *Chem. – Eur. J.*, 2011, **17**, 7069–7079.
25 M. Vougo-Zanda, J. Huang, E. Anokhina, X. Wang and A. J. Jacobson, *Inorg. Chem.*, 2008, **47**, 11535–11542.
26 A. R. B. J. Lutton-Gething, L. T. Nangkam, J. O. W. Johansson, I. Pallikara, J. M. Skelton, G. F. S. Whitehead, I. Vitorica-Yrezabal and M. P. Attfield, *Chem. – Eur. J.*, 2023, **29**, e202203773.
27 O. V. Dolomanov, L. J. Bourhis, R. J. Gildea, J. A. K. Howard and H. Puschmann, *J. Appl. Crystallogr.*, 2009, **42**, 339–341.
28 G. M. Sheldrick, *Acta Crystallogr., Sect. A*, 2008, **64**, 112–122.
29 G. M. Sheldrick, *Acta Crystallogr., Sect. A*, 2015, **71**, 3–8.
30 G. M. Sheldrick, *Acta Crystallogr., Sect. C: Struct. Chem.*, 2015, **71**, 3–8.
31 A. L. Spek, *Acta Crystallogr., Sect. C: Struct, Chem*, 2015, **71**, 9–18.
32 A. A. Coelho, *J. Appl. Crystallogr.*, 2018, **51**, 210–218.
33 H. G. Harvey, A. C. Herve, H. C. Hailes and M. P. Attfield, *Chem. Mater.*, 2004, **16**, 3756–3766.
34 B. E. G. Zhang, V. V. Lucier, R. Terskikh, Zheng and Y. Huang, *Solid State Nucl. Magn. Reson.*, 2017, **84**, 118–131.
35 G. Chaplais, A. Simon-Masseron, F. Porcher, C. Lecomte, D. Bazer-Bachi, N. Bats and J. Patarin, *Phys. Chem. Chem. Phys.*, 2009, **11**, 5241–5245.
36 F. Millange, N. Guillou, R. I. Walton, J. M. Grenèche, I. Margiolaki and G. Férey, *Chem. Commun.*, 2008, 4732–4734.
37 F. Millange, N. Guillou, M. E. Medina, G. Férey, A. Carlin-Sinclair, K. M. Golden and R. I. Walton, *Chem. Mater.*, 2010, **22**, 4237–4245.
38 P. L. Llewellyn, P. Horcajada, G. Maurin, T. Devic, N. Rosenbach, S. Bourrelly, C. Serre, D. Vincent, S. Loera-Serna, Y. Filinchuk and G. Férey, *J. Am. Chem. Soc.*, 2009, **131**, 13002–13008.

39 M. Agrawal, S. Bhattacharyya, Y. Huang, K. C. Jayachandrababu, C. R. Murdock, J. A. Bentley, A. Rivas-Cardona, M. M. Mertens, K. S. Walton, D. S. Sholl and S. Nair, *J. Phys. Chem. C*, 2018, **122**, 386–397.
40 (*a*) CCDC 2468139: Experimental Crystal Structure Determination, 2025, DOI: **10.5517/ccdc.csd.cc2nv9d7**; (*b*) CCDC 2468140: Experimental Crystal Structure Determination, 2025, DOI: **10.5517/ccdc.csd.cc2nv9f8**; (*c*) CCDC 2468141: Experimental Crystal Structure Determination, 2025, DOI: **10.5517/ccdc.csd.cc2nv9g9**; (*d*) CCDC 2468142: Experimental Crystal Structure Determination, 2025, DOI: **10.5517/ccdc.csd.cc2nv9hb**.